ELSEVIER

Journal of Nuclear Materials 254 (1998) 175–184

journal of nuclear materials

X-ray absorption fine structure of aged, Pu-doped glass and ceramic waste forms

N.J. Hess [a,*], W.J. Weber [a], S.D. Conradson [b]

[a] *Pacific Northwest National Laboratory, PO Box 999, MS K2-44, Richland, WA 99352, USA*
[b] *Los Alamos National Laboratory, MS D429, Los Alamos, NM 87545, USA*

Received 2 September 1997; revised 2 January 1998

Abstract

X-ray absorption spectroscopic (XAS) studies were performed on three compositionally identical, Pu-doped, borosilicate glasses prepared 15 years ago at different α-activities by varying the $^{239}Pu/^{238}Pu$ isotopic ratio. The resulting α-activities ranged from 1.9×10^7 to 4.2×10^9 Bq/g and have current, accumulated doses between 8.8×10^{15} to 1.9×10^{18} α-decays/g. Two ceramic, polycrystalline zircon ($ZrSiO_4$) samples prepared 16 years ago with 10.0 wt% Pu was also investigated. Varying the $^{239}Pu/^{238}Pu$ isotopic ratio in these samples resulted in α-activities of 2.5×10^8 and 5.6×10^{10} Bq/g and current, accumulated doses of 1.2×10^{17} and 2.8×10^{19} α-decays/g. The multicomponent composition of the waste forms permitted XAS investigations at six absorption edges for the borosilicate glass and at three absorption edges for the polycrystalline zircons. For both waste forms, analysis of extended X-ray absorption fine structure (EXAFS) and X-ray absorption near edge structure (XANES) spectra indicates that the local environment around the cations exhibits different degrees of disorder as a result of the accumulated α-decay dose. In general, cations with short cation-oxygen bonds show little effect from self-radiation whereas cations with long cation–oxygen bonds show a greater degree of disorder with accumulated α-decay dose. © 1998 Elsevier Science B.V.

PACS: 61.80.−x; 61.10.Ht; 23.60.+e; 28.41.Kw

1. Introduction

Waste forms currently under consideration for permanent deposition of radioactive, high-level waste include lanthanide borosilicate glass and ceramic hosts. The radiation effects on the stability and durability of these waste forms have been actively pursued and yet there is little fundamental understanding of the radiation-damage processes. As a result, extrapolations based on the limited understanding of damage accumulation to highly radioactive waste forms, such as that generated by HLW processing or the incorporation of weapons-grade plutonium, are tenuous. The samples studied here include three aged, borosilicate glasses in which the accumulated α-decay dose varies by a factor of 200 and a pair of plutonium-doped, polycrystalline zircon samples, one of which is highly crystalline and the other is rendered amorphous by the effects of α-decay. The significance of these samples is that the cumulative α-decay doses are within the range calculated for proposed waste forms containing weapons-grade plutonium. At this time, no other aged samples with doses within this range have been studied in detail, particularly with respect to structural changes at the molecular level.

Beta and alpha decay of incorporated radionuclides affect waste forms through the interactions of β-particles,

* Corresponding author. Tel.: +1-509 376 9808; fax: +1-509 376 1321; e-mail: nj_hess@pnl.gov.

PII S0022-3115(98)00011-7

α-particles, α-recoil nuclei, and γ-rays with atoms in the materials. These interactions can be characterized as either ionizing, involving the transfer of energy to electrons, or as ballistic, involving the transfer of energy to the nuclei via elastic collisions. For β-particles and γ-rays, the ionization process dominates; for α-particles and recoil nuclei the velocity of the ions determines whether the interaction is predominately ionizing or ballistic in character.

Ballistic processes cause direct atomic displacements through elastic scattering collisions and are responsible for atomic-scale rearrangement of the structure. In most ceramic oxides, ballistic processes are the principal mechanism of defect production. Alpha decay results in the formation of high-energy α-particles (4 to 6 MeV) and energetic α-recoil nuclei (70 to 100 keV). The α-particles dissipate most of their energy by ionization processes along a path length of 16 to 22 μm. In addition, α-particles participate in ballistic collisions that generate 200 to 400 atomic displacements per decay, with the highest density of displacements occurring near the end of the α-particle path. The more massive but lower energy α-recoil particles account for most of the atomic displacements produced in solid waste forms. Alpha-recoil particles have a much shorter path length, 30 to 40 nm, but generate in 1000 to 2000 atomic displacements per decay which can result in local melting and disorder. In fact, leaching studies using isotopic analysis have shown that daughter products are twice as likely to be leached from a highly-irradiated waste form than the parent actinide as a result of the damage created by the α-decay event and the ballistic propagation of the daughter through the waste form [1,2].

X-ray absorption spectroscopy (XAS) is an ideal technique to address the effects of accumulated α-decay dose because XAS is sensitive to changes in short-range order such as the oxidation state, the identity of coordinating atoms, and the geometry of the coordination environment of the parent actinides (e.g., ^{239}Pu) and their daughter products (e.g., ^{235}U). However, the interpretation of XAS data in self-radiation studies requires careful analysis, especially at low accumulated doses. At low accumulated α-decay doses, the atomic displacements produced by α-decay form highly-localized, isolated regions called damage cascades [3,4]. Within a damage cascade, atoms can reside in a distorted coordination environment. Outside a damage cascade, atoms generally remain in a pristine environment. Because XAS samples all the absorbing atoms in the sample equivalently, the measured spectra represents the average of all the atom's coordination environments, both distorted and pristine. At low accumulated doses the number of atoms within damage cascade regions will be small and the measured XAS spectra will be dominated by the atoms in pristine, unaffected regions. At high accumulated doses, the damage cascade regions overlap and material is uniformly disordered or amorphous. In this scenario, the measured XAS spectra will reflect the disordered state of the material.

2. Experimental

The composition of the borosilicate glass, given in Table 1, is similar to the defense reference waste glass [5]. Three compositionally-identical glass samples were prepared in July 1982 with 1 wt% PuO_2, in which the variation in ^{238}Pu/^{239}Pu isotopic composition resulted in a 200-fold variation in the accumulated dose [5]. The zircon samples were prepared in August 1981 with 8.1 mol% of zirconium replaced with ^{239}Pu or ^{238}Pu [6]. The resulting accumulated α-decay doses are given in Table 2. For EXAFS analysis, the glass samples were cut from 30 g bars and friction fit into the sample holder. The polycrystalline zircon samples were first powdered, mixed with a collodion–amyl acetate solution, and loaded into the sample holder as a slurry.

EXAFS measurements were conducted at the Stanford Synchrotron Radiation Laboratory under dedicated operating conditions (3.0 GeV and 40 to 90 mA current). Spectra were collected at the Pu and U L_{III}-edges and the Mn, Fe, Sr and Zr K-edges in transmission and fluorescence modes simultaneously up to a photoelectron wavevector of 1.3 nm^{-1} at 77 K. The transmission spectrum was measured using standard ionization chamber detectors, while the fluorescence spectrum was measured using a 13-element Ge detector. Energy calibration for the Mn and Fe edges was performed by assigning the first inflection point in the absorption edge of an Fe foil to 7111.30 eV. Similarly, the Sr, Zr, U, and Pu edges were calibrated by assigning the first inflection point in the absorption edge of a Zr foil to 17 999.35 eV. The absorption spectrum was normalized by fitting polynomials through the pre- and post-edge regions. At E_0, the value of the extrapolated pre-edge was set to zero and the difference between the extrapolations of the pre- and post-edge polynomials was set to unity.

Table 1
Composition of waste glass

Oxide	Wt%
SiO_2	50.6
Fe_2O_3	10.0
Na_2O	9.1
B_2O_3	7.0
Al_2O_3	6.0
Li_2O_3	4.9
MnO_2	3.0
U_3O_8	3.0
CaO	2.0
NiO	2.0
PuO_2	1.0
MgO	0.7
ZrO_2	0.7
Cs_2O	0.5
SrO	0.5

Table 2
Sample isotopic composition and accumulated α-decay dose

Sample	Pu isotopic composition	Accumulated dose (α-decays/g)
DRG-P1 glass	1.0 wt% $^{239}PuO_2$	8.8×10^{15}
DRG-P2 glass	0.9 wt% $^{239}PuO_2$, 0.1 wt.% $^{238}PuO_2$	2.0×10^{17}
DRG-P3 glass	1.0 wt% $^{238}PuO_2$	1.9×10^{18}
^{239}Pu-doped zircon	10.0 wt% ^{239}Pu	1.2×10^{17}
^{238}Pu-doped zircon	8.85 wt% ^{238}Pu, 1.15 wt.% ^{239}Pu	2.8×10^{19}

XANES can be used to determine the oxidation state of the absorbing element by measuring the energy shift of the absorption edge. With higher oxidation states, the absorption edge shifts to higher energy by a few eV. In addition, the shape of the XANES profile often reflects the geometry of the first coordination sphere of many transition and actinide elements and can be used to assess qualitatively the coordination environment of the absorbing atom. For

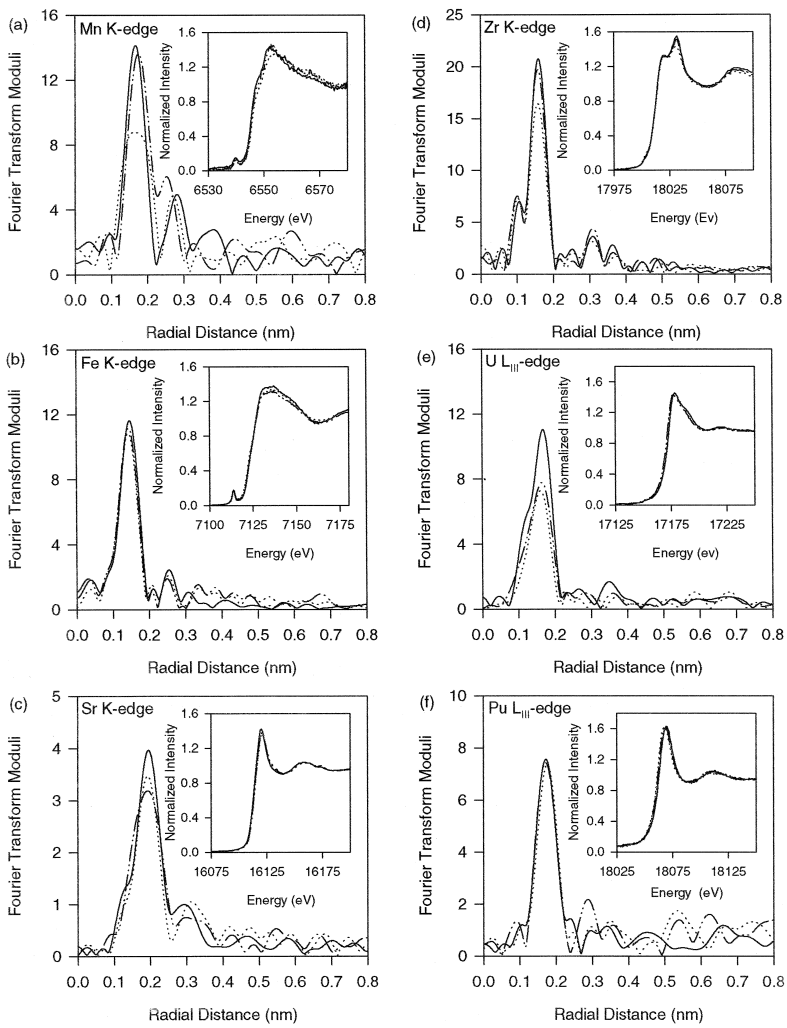

Fig. 1. Results for waste glass. The Fourier transform of the EXAFS and XANES, the latter shown in inset, of the waste glass samples. The solid line is DRG-P1, the dashed line is DRG-P2, and the dotted line is DRG-P3. (a) Mn K-edge, (b) Fe K-edge, (c) Sr K-edge, (d) Zr K-edge, (e) U L_{III}-edge, and (f) Pu L_{III}-edge.

instance, a shoulder on the high energy side of the absorption edge appears with the formation of the very short axial bonds that define the uranyl and plutonyl configurations. This trans-dioxo cation moiety occurs in the (V) and (VI) oxidation states of uranium and plutonium but not in the (III) and (IV) oxidation states.

Analysis of the EXAFS oscillations provides quantitative information on the number and chemical identity of neighboring atoms as well as their distance from the absorber. The EXAFS oscillations were extracted by fitting a polynomial spline function through the post-edge region and normalizing the difference between this approximation of the solitary-atom EXAFS and the actual data with the absorption decrease calculated using the McMaster tables [7]. Fourier transforms were taken over photoelectron wavevector ranges that varied on the basis of the signal-to-noise ratio for each element. EXAFS nodes were selected as endpoints to the Fourier transform range and a two-sigma-wide Gaussian window was used to dampen the EXAFS oscillations at the endpoints. The resulting Fourier transforms of the glass and the zircon samples are shown in Figs. 1 and 2, respectively. The phase shift has not been removed from the Fourier transforms and as a result the peaks in the transform moduli in these figures appear 0.02 to 0.05 nm shorter than the actual distance from the absorber to the neighboring atoms.

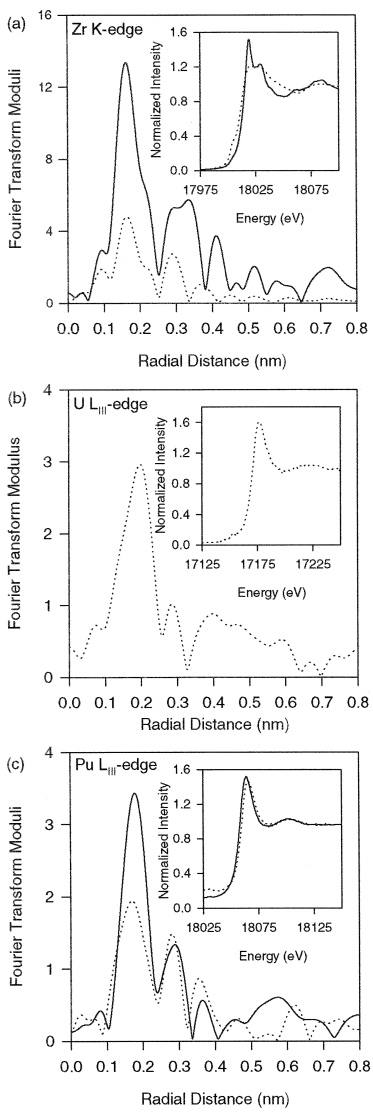

Fig. 2. Results for zircon. The Fourier transform of the EXAFS and XANES, the latter shown in inset, of the polycrystalline zircon samples. The solid line is the ^{239}Pu-doped zircon sample and the dotted line is the ^{238}Pu-doped zircon sample. (a) Zr K-edge, (b) U L_{III}-edge, and (c) Pu L_{III}-edge.

The phase and amplitude for the cation-oxygen and cation-silicon scattering paths were calculated using the ab initio code FEFF7.02 [8,9]. These individual scattering paths were then parameterized and used to fit the experimentally measured EXAFS. The crystalline silicates rhodonite ($MnSiO_4$) [10], Sr_2SiO_4 [11], zircon ($ZrSiO_4$) [12], coffinite ($USiO_4$) [13], and $PuSiO_4$ [14] were used to approximate the local cation environment in the waste forms and were used as input for FEFF7.02. To calculate scattering paths for tetrahedral iron in a silicate framework, iron was substituted for aluminum in the aluminosilicate microcline ($KAlSi_3O_8$) [15]. In addition, the uranium triscarbonato complex [16] was used as the model for the trans-dioxo cation, U–O_{td}, and for the multiple scattering contributions, U–ms.

3. Results

3.1. Simulated waste glass

The XANES of the glass samples are shown as insets in Fig. 1. Although all of the XANES spectra show slight variation in the shape of the XANES profile or the energy of the absorption edge, these variations are most likely the result of structural changes due to radiation-damage rather than oxidation state changes. The U L_{III}-edge XANES may be an exception as discussed below. The absorption edge energy readily indicates the oxidation state of elements. This is particularly useful for elements with multiple oxidation states. From measurements of the absorption edge energies, the oxidation state of the metal cations in the glass samples is determined to be as follows: Mn^{2+}, Fe^{3+}, Sr^{2+}, Zr^{4+}, and Pu^{4+}. At the U L_{III}-edge, all the glass samples exhibit the shoulder typical of the formation of the trans-dioxo cation suggesting the presence of U^{6+} However, the measured uranium absorption edge energy falls within an energy range that is consistent with U^{4+}. Previous studies of uranium in glass have also reported similar shoulder features and a shift of the absorption edge to lower energies than expected for U^{6+} [17–21]. In these

studies, analysis of the U L_{III}-edge EXAFS revealed a distribution of bond lengths that were intermediate between the short U–O bond lengths typical of U^{4+} compounds and the longer equatorial U–O bond lengths characteristic of U^{6+} compounds. In this intermediate environment it appears that the absorption edge energy of uranium is influenced both by its coordination environment and its oxidation state. Note that the DRG-P2 and DRG-P3 glasses exhibit a decrease in the height of the trans-dioxo shoulder suggesting that the amount of U^{6+} present in these glasses is less than that in the DRG-P1 glass. The apparent decrease in the amount of U^{6+} in the DRG-P2 and DRG-P3 glasses is surprising because α-particles lose 95% of their energy through inelastic interactions which are largely ionizing [6] and should promote oxidation. One explanation is that the oxygen fugacity during synthesis of the three glass samples was not identical and the current U^{6+} concentration reflects a variation in synthesis conditions and not oxidation state changes due to radiation-damage processes. Another explanation maybe the evolution of O_2, which is known to occur in borosilicate glasses under ionizing radiation [3].

Fourier transforms of the EXAFS oscillations are shown in Fig. 1. With the exception of the Fe and Pu edges, the Fourier transforms of the EXAFS display a progressive decrease in the amplitude of the oxygen nearest-neighbor shell with increasing accumulated dose. The amplitude decrease is likely due to an increase in the disorder of the oxygen shell with increasing accumulated dose rather than a reduction in the number of oxygen atoms. Fitting results to the EXAFS are given in Table 3 and are discussed for each edge below.

Fits to the Mn K-edge EXAFS reveal both an increase in the disorder and the appearance of a second Mn–O bond distance with accumulated α-decay dose. Evidence for a rearrangement of the Mn–O bond lengths can also be observed in the changing shape of the XANES profile. The Mn–O bond distance of 0.208 nm is slightly longer than the typical octahedral Mn^{3+}–O bond distance of 0.202 nm [22] but shorter than typical octahedral Mn^{2+}–O bond distance of 0.221 nm [22] for crystalline structures. However, 0.208 nm is typical of Mn–O bonds in borosilicate glasses with similar composition.

The fitted Fe–O bond distance of 0.190 nm and number of first neighbor oxygen atoms, around four, is consistent with tetrahedral coordination of Fe^{3+}. Tetrahedral Fe^{3+} in Na-silicate glass has been observed by Calas and Petiau [23]. Corroborating evidence for tetrahedral coordinated Fe is also apparent in the large intensity of the pre-edge peak in the Fe K-edge XANES show in Fig. 1(b). Slight decreases in the Fe–O and Fe–Si bond distances are observed with increasing accumulated α-decay dose. Except for the these minor changes, the accumulated dose has little effect on the Fe coordination environment.

Fits to the Sr K-edge EXAFS reveals that the peak in the Fourier transform is composed of a Sr–O bond at 0.258 nm, a distance consistent with eight-coordinate Sr in crystalline silicates [22]. As a result, the fits were performed fixing the number of first-shell oxygen atoms at 8 and allowing the bond distance and the disorder to vary. A slight decrease in the Sr–O bond distance and an increase in the disorder is observed with increasing accumulated α-decay dose.

Fits to the Zr K-edge EXAFS reveal that zirconium is coordinated by eight oxygen atoms at 0.209 nm. This bond distance is 0.01 nm shorter than the average Zr–O bond distance of approximately 0.220 nm in a crystalline oxide host [22]. The zirconium site shows little change in bond distance with accumulated α-decay dose; however, the disorder increases for the highest dose glass, DRG-P3. The next-nearest neighbor Zr–Si shells exhibit little change with increasing accumulated α-decay dose.

Analysis of the U L_{III}-edge EXAFS reveals a decrease in the number of trans-dioxo atoms at approximately 0.18 nm with increasing accumulated dose and a decrease in the corresponding multiple scattering contribution at approximately 0.35 nm. The decrease in the number of trans-dioxo oxygen atoms suggests that the concentration of U^{6+} is reduced in the DRG-P2 and DRG-P3 glasses, an interpretation that is consistent with the decrease in trans-dioxo atoms observed in the XANES. In addition, the lowest dose glass, DRG-P1, exhibits a Fourier transform peak at approximately 0.35 nm which corresponds to a U–U scattering path at 0.362 nm. This peak suggests the presence of polymeric, multinuclear uranium species. The occurrence of polymeric uranium in a glass that contains only 3.0 wt% U_3O_8 indicates that uranium is not uniformly dispersed and that uranium-rich domains or clusters are formed. Uranium-rich clusters in glass of similar composition has also been observed by Greaves [20]. The absence of a U–U scattering path in the higher dose glasses, suggesting the absence of uranium polymeric species, may reflect possible differences in synthesis conditions noted earlier and not the effect of accumulated α-decay damage.

The Fourier transforms of the Pu L_{III}-edge EXAFS shown in Fig. 1(f) display a single Pu–O scattering path. However, fitting the EXAFS reveals the Pu–Si and Pu–O contributions. The fitting results in Table 3 show little change in the number of atoms or the disorder, sigma, of the Pu–O shell with accumulated dose of the waste glass samples. However, the next nearest neighbor shells consisting of Pu–Si, contracts significantly with increasing accumulated α-decay dose.

3.2. Zircon

The Zr K-edge and U and Pu L_{III}-edge XANES spectra of the polycrystalline zircon samples are shown as insets in Fig. 2. All the uranium present in the ^{238}Pu-doped zircon formed as the daughter product of ^{238}Pu decay. Because the half-life of ^{239}Pu is much longer than that of ^{238}Pu, only trace amounts of uranium are present in the ^{239}Pu-

doped zircon. As a result, U L_{III}-edge XAS was only collected on the ^{238}Pu-doped zircon. The absorption edge energy in the XANES indicates that the oxidation state of uranium in the ^{238}Pu-doped zircon is U^{4+} and the plutonium in both zircon samples is Pu^{3+}. The replacement of 8.1 mol% of Zr^{4+} with Pu^{3+} means that both zircon samples are slightly oxygen deficient. The significant differences between the Zr K-edge XANES of ^{239}Pu- and ^{238}Pu-doped zircon reflect a major structural rearrangement of the average zirconium local environment due to the accumulated α-decay dose.

Fourier transforms of the Zr K-edge, U and Pu L_{III}-edge EXAFS shown in Fig. 2a–c exhibit significant differences between the highly-crystalline ^{239}Pu-doped zircon and the

Table 3
(a) EXAFS fitting results at Mn K-edge for waste glass

		Mn–O[a]	Mn–O	Mn–Si	Mn–Si	Mn–O
DRG-P1	distance	0.208 ± 0.003		0.325 ± 0.002		0.420 ± 0.002
	number	5.0 ± 1.3		2.1 ± 0.7		4.6 ± 1.4
$r^2 = 0.9824$	sigma	0.09 ± 0.02		0.00 ± 0.00		0.00 ± 0.00
DRG-P2	distance	0.208 ± 0.003	0.251 ± .0002	0.321 ± 0.002	0.343 ± 0.002	
	number	4.6 ± 1.3	1.5 ± 0.5	1.5 ± 0.5	0.5 ± 0.1	
$r^2 = 1.3796$	sigma	0.07 ± 0.03	0.00 ± 0.00	0.00 ± 0.00	0.01 ± 0.00	
DRG-P3	distance	0.203 ± 0.004	0.256 ± 0.002	0.318 ± 0.002		
	number	5.5 ± 0.3	1.7 ± 0.5	2.1 ± 0.7		
$r^2 = 0.9937$	sigma	0.12 ± 0.02	0.00 ± 0.00	0.00 ± 0.00		

(b) EXAFS fitting results at Fe K-edge for waste glass

		Fe–O[b]	Fe–Si	Fe–Si	Fe–O
DRG-P1	distance	0.190 ± 0.002	0.308 ± 0.002	0.327 ± 0.002	0.360 ± 0.002
	number	3.4 ± 0.7	1.0 ± 0.3	1.1 ± 0.3	1.0 ± 0.3
$r^2 = 0.5393$	sigma	0.08 ± 0.00	0.00 ± 0.00	0.04 ± 0.6	0.00 ± 0.00
DRG-P2	distance	0.189 ± 0.002	0.307 ± 0.002	0.327 ± 0.002	0.365 ± 0.002
	number	3.0 ± 0.7	0.9 ± 0.2	0.8 ± 0.3	1.3 ± 0.4
$r^2 = 0.7055$	sigma	0.07 ± 0.02	0.00 ± 0.00	0.00 ± 0.00	0.00 ± 0.00
DRG-P3	distance	0.188 ± 0.002	0.304 ± 0.002	0.321 ± 0.002	
	number	2.9 ± 0.7	0.6 ± 0.2	1.0 ± 0.3	
$r^2 = 0.7107$	sigma	0.07 ± 0.02	0.00 ± 0.00	0.09 ± 0.2	

(c) EXAFS fitting results at Sr K-edge for waste glass

		Sr–O[c]	Sr–Si	Sr–O
DRG-P1	distance	0.256 ± 0.002	0.341 ± 0.002	0.427 ± 0.003
	number	8.0, fixed	1.1 ± 0.5	1.6 ± 0.5
$r^2 = 0.3657$	sigma	0.10 ± 0.02	0.10 ± 0.02	0.10 ± 0.02
DRG-P2	distance	0.254 ± 0.002	0.341 ± 0.002	0.427 ± 0.002
	number	8.0, fixed	0.9 ± 0.2	2.1 ± 0.4
$r^2 = 0.4341$	sigma	0.11 ± 0.02	0.10 ± 0.02	0.10 ± 0.03
DRG-P3	distance	0.252 ± 0.002	0.341 ± 0.002	0.427 ± 0.002
	number	8.0, fixed	0.9 ± 0.1	3.2 ± 0.7
$r^2 = 0.3815$	sigma	0.12 ± 0.02	0.10 ± 0.03	0.10 ± 0.03

(d) EXAFS fitting results at Zr K-edge for waste glass

		Zr–O[d]	Zr–Si	Zr–Si	Zr–O
DRG-P1	distance	0.209 ± 0.002	0.295 ± 0.002	0.375 ± 0.002	0.413 ± 0.002
	number	7.0 ± 1.5	1.1 ± 0.3	3.0 ± 0.9	6.0 ± 1.8
$r^2 = 0.8387$	sigma	0.08 ± 0.02	0.09 ± 0.02	0.07, fixed	0.06, fixed
DRG-P2	distance	0.209 ± 0.002	0.295 ± 0.002	0.373 ± 0.002	0.416 ± 0.002
	number	7.1 ± 1.6	0.8 ± 0.3	3.2 ± 0.9	3.7 ± 1.2
$r^2 = 0.8812$	sigma	0.08 ± 0.01	0.10 ± 0.02	0.07, fixed	0.06, fixed
DRG-P3	distance	0.209 ± 0.002	0.293 ± 0.002	0.375 ± 0.002	0.412 ± 0.002
	number	6.8 ± 1.6	0.8 ± 0.3	2.2 ± 0.7	2.8 ± 0.9
$r^2 = 0.8543$	sigma	0.10 ± 0.02	0.06 ± 0.02	0.07, fixed	0.06, fixed

Table 3 (continued)

(e) EXAFS fitting results at U L_{III}-edge for waste glass

		U–O_{tr} [e]	U–O_{eq}	U–O	U–ms	U–U
DRG-P1	distance	0.183 ± 0.002	0.221 ± 0.002	0.274 ± 0.003	0.350 ± 0.003	0.362 ± 0.002
	number	1.8 ± 0.5	5.7 ± 0.4	1.9 ± 0.6	1.1 ± 0.3	1.9 ± 0.5
$r^2 = 0.7053$	sigma	0.01, fixed	0.08, fixed	0.10, fixed	0.02 ± 0.07	0.07 ± 0.02
DRG-P2	distance	0.179 ± 0.002	0.224 ± 0.002		0.351 ± 0.003	0.362 ± 0.002
	number	1.1 ± 0.3	4.5 ± 1.2		2.9 ± 0.9	
$r^2 = 0.8169$	sigma	0.01, fixed	0.08, fixed		0.08 ± 0.03	
DRG-P3	distance	0.180 ± 0.002	0.222 ± 0.002		0.350 ± 0.004	
	number	1.0 ± 0.3	3.7 ± 1.0		1.7 ± 0.5	
$r^2 = 0.6958$	sigma	0.01, fixed	0.08, fixed		0.10 ± 0.03	

(f) EXAFS fitting results at Pu L_{III}-edge for waste glass

		Pu–O [f]	Pu–Si	Pu–O
DRG-P1	distance	0.223 ± 0.002	0.311 ± 0.002	0.388 ± 0.002
	number	6.7 ± 1.8	0.3 ± 0.1	2.9 ± 0.9
$r^2 = 1.0735$	sigma	0.09, fixed	0.00 ± 0.00	0.00 ± 0.02
DRG-P2	distance	0.223 ± 0.003	0.305 ± 0.002	0.371 ± 0.002
	number	6.0 ± 1.7	0.9 ± 0.3	2.7 ± 0.8
$r^2 = 1.4705$	sigma	0.09, fixed	0.00 ± 0.00	0.00 ± 0.00
DRG-P3	distance	0.223 ± 0.003	0.298 ± 0.002	
	number	6.3 ± 1.8	0.4 ± 0.1	
$r^2 = 1.6962$	sigma	0.09, fixed	0.00 ± 0.04	

[a] E_0 for Mn K-edge is defined as 6535 eV. ΔE_0 for these shells is 11.5 eV.
[b] E_0 for Fe K-edge is defined as 7112 eV. ΔE_0 for these shells is −3.5 eV.
[c] E_0 for Sr K-edge is defined as 16125.0 eV. ΔE_0 for these shells is 1.0 eV.
[d] E_0 for Zr K-edge is defined as 18010 eV. ΔE_0 for these shells is 1.1 eV.
[e] E_0 for U L_{III}-edge is defined as 17170 eV. ΔE_0 for these shells is 5 eV.
[f] E_0 for Pu L_{III}-edge is defined as 18060 eV. ΔE_0 for these shells is 6 eV.

fully-amorphous ^{238}Pu-doped zircon. Fitting results for the EXAFS are given in Table 4. Within the zircon structure, zirconium is coordinated by four oxygen atoms at 0.213 nm and four oxygen atoms at 0.227 nm [12]. The fitted Zr–O bond distance of 0.217 nm for the ^{239}Pu-doped zircon is similar to the average value for pristine zircon, 0.220 nm. Indeed, due to the high crystallinity of this sample, shells up to 0.60 nm from the absorber are fit. In contrast, the fitted Zr–O bond distance of 0.204 nm for the ^{238}Pu-doped zircon shows little agreement with the Zr–O bond distances for zircon but is quite similar to bond distances reported for the monoclinic form of ZrO_2, baddeleyite [24]. The fitted distance is also similar to that determined by Farges and Calas [25] in their study of natural metamict zircon crystals. The Zr–Zr correlations determined for the ^{238}Pu-doped zircon at 0.345 nm and 0.396 nm are also consistent with the baddeleyite structure. Baddeleyite is the thermodynamically stable form of ZrO_2. and its presence could reflect residual oxide components from synthesis. However, no residual ZrO_2 or SiO_2 were observed in the initial XRD analysis of the ^{238}Pu-doped zircon following synthesis. Instead, it is likely that the high accumulated α-decay dose experienced by the zircon has significantly rearranged the Zr cations and the isolated SiO_4 tetrahedra to produce shorter Zr–O bond lengths and Zr–Zr correlations. Neutron scattering experiments are planned to more thoroughly investigate the details of the structural rearrangement in the ^{238}Pu-doped zircon.

Fits to the U L_{III}-edge EXAFS indicate that there are two U–O shells separated by approximately 0.02 nm, a configuration typical of U^{4+} oxides. However, these bond lengths are too short to be consistent with a model in which the uranium atom forms a coffinite-like structure, the U-silicate analog of zircon. The short bond lengths and the small number of oxygen atoms in these two shells suggest that uranium is sitting in a highly disordered site. The high degree of disorder around uranium atoms is expected since uranium is the massive α-recoil particle of plutonium α-decay and therefore resides within the damage cascade created as it traveled ballistically through the lattice.

Analysis of the Pu L_{III}-edge EXAFS reveals that the local environment around the Pu atoms is similar to that calculated for the Pu-silicate analog of zircon, $PuSiO_4$. In the calculated structure, there are two Pu–O shells separated by 0.02 nm. The fitted Pu–O bond distances of 0.221 nm and 0.239 nm for the highly-crystalline zircon are about 0.010 nm shorter than the calculated values for

Table 4
(a) EXAFS fitting results at Zr K-edge for zircon

	Near shells	Zr–O[a]	Zr–Si	Zr–Si	Zr–Zr	Zr–Zr/Si
Zircon	distance	0.220 ± 0.007	0.299 ± 0.000			0.366 ± 0.002
Literature	number	8	2			4.0/4.0
^{239}Pu zircon	distance	0.217 ± 0.002	0.298 ± 0.002			
	number	7.8 ± 1.8	1.3 ± 0.4			2.3 ± 0.6
	sigma	0.10 ± 0.02	0.00 ± 0.00			0.04 ± 0.02
	distal shells	Zr–O	Zr–O/ms	Zr–Si	Zr–Zr/Sr	Zr–Zr
Zircon	distance	0.405 ± 0.000	0.454 ± 0.000	0.467 ± 0.000	0.555 ± 0.002	0598 ± 0.00
Literature	number	8	4	4	12.0/4.0	2
^{239}Pu zircon	distance	0.403 ± 0.002	0.459 ± 0.002	0.470 ± 0.002	0.556 ± 0.002	0.608 ± 0.002
	number	4.0 ± 1.2	6.8 ± 2.0	2.0 ± 0.6	4.5 ± 1.3	2.6 ± 0.8
$r^2 = 0.9783$	sigma	0.01 ± 0.00	0.06 ± 0.02	0.00 ± 0.00	0.00 ± 0.00	0.03 ± 0.06
		Zr–O[a]	Zr–O		Zr–Zr	Zr–Zr
Baddeleyite	distance	0.210 ± 0.007	0.223 ± 0.004		0.348 ± 0.004	0.396 ± 0.005
Literature	number	4	3		5	4
^{238}Pu zircon	distance	0.204 ± 0.002	0.212 ± 0.003		0.338 ± 0.002	0.415 ± 0.002
	number	4.2 ± 2.0	1.9 ± 0.5		3.4 ± 1.0	1.4 ± 0.5
$r^2 = 0.6017$	sigma	0.16 ± 0.02	0.09 ± 0.02		0.13 ± 0.01	0.12 ± 0.01

(b) EXAFS fitting results at U L_{III}-edge for zircon

		U–O[b]	U–O
^{238}Pu zircon	distance	0.214 ± 0.003	0.235 ± 0.002
	number	1.7 ± 0.5	3.0 ± 1.0
$r^2 = 1.1532$	sigma	0.06, fixed	0.06, fixed

(c) EXAFS fitting results at Pu L_{III}-edge for zircon

		Pu–O[c]	Pu–O	Pu–Si	Pu–Si/Zr	Pu–O
$PuSiO_4$	distance	0.229 ± 0.000	0.249 ± 0.000	0.311 ± 0.000	0.378 ± 0.000	0.421 ± 0.000
Literature	number	4	4	2	4.0/4.0	8
^{239}Pu zircon	distance	0.221 ± 0.002	0.239 ± 0.002	0.316 ± 0.002	0.364 ± 0.002	0.415 ± 0.002
	number	2.9 ± 0.8	4.7 ± 1.2	1.0 ± 0.3	6.6 ± 2.0	3.0 ± 1.2
$r^2 = 0.4132$	sigma	0.00 ± 0.00	0.00 ± 0.00	0.07 ± 0.02	0.14 ± 0.02	0.00 ± 0.00
^{238}Pu zircon	distance		0.232 ± 0.006	0.317 ± 0.002	0.366 ± 0.003	0.406 ± 0.002
	number		8.0 ± 2.3	1.2 ± 0.4	3.1 ± 1.0	3.1 ± 1.2
$r^2 = 0.4633$	sigma		0.15 ± 0.02	0.14 ± 0.02	0.14 ± 0.02	0.00 ± 0.00

[a] E_0 for Zr K-edge is defined as 18010 eV. ΔE_0 for these shells is 2.0 eV.
[b] E_0 for U L_{III}-edge is defined as 17170 eV. ΔE_0 for these shells is 5 eV.
[c] E_0 for Pu L_{III}-edge is defined as 18060 eV. ΔE_0 for these shells is 3 eV.

$PuSiO_4$. The average distance is approximately 0.015 nm longer than the observed Zr–O bond length in the ^{239}Pu-doped zircon. However, the bond distances determined for the next-nearest neighbor Zr–Zr/Si and Pu–Zr/Si shells at 0.365 nm are identical. These results suggest that the substitution of Pu^{3+} for Zr^{4+} in the zircon structure creates highly-localized distortion around the Pu atom that is dissipated at a distance of approximately 0.35 nm. The single Pu–O bond distance of 0.232 nm determined for the fully-amorphous zircon is nearly equal to the average of the two Pu–O distances determined for the highly-crystalline zircon, suggesting that the oxygen atoms are more disordered. The bond distances determined for the Pu–Si and Pu–Si/Zr next-nearest neighbor shells are identical to those determined for the highly-crystalline zircon. The preservation of the Pu environment in the fully-amorphous zircon suggests that this configuration is stable at high accumulated α-decay doses.

4. Discussion

Analysis of the XAS spectra suggests that the response to self-radiation damage in the glass and ceramic waste forms with accumulated α-decay dose is not uniform for all the elements investigated in this study. Some cations,

such as Fe, exhibit small effects whereas other cations, such as Mn and U, display large effects. Indeed, the latter two cations are the most sensitive to α-decay showing increased disorder and changes in the oxygen atom distribution over cation–oxygen bond distances. To interpret the individual responses to radiation damage it is useful to consider the role that the cations play in the glass structure. In the waste glasses, Fe is tetrahedrally coordinated by oxygen forming tetrahedral units analogous to the SiO_4 tetrahedra. The tetrahedral units link together to form the glass network. As such, Fe is considered a network-former in the glass structure. In previous radiation damage studies on glasses and silicates [26,27], the tetrahedral unit is the structural element commonly observed to be resistant to radiation damage whereas the glass network is seen to undergo structural changes. The radiation damage resistance can be ascribed to the short cation–oxygen bond lengths and the covalent character of the bond.

Larger cations, such as some transition metals, alkali earths–alkali metals, and the actinides, are too large to substitute into the silicate framework and are called network-modifiers because they prevent tetrahedral units from forming complete linkages. Generally, the largest cations such as Sr, U, Pu, and Zr are coordinated by eight or more oxygen atoms. As a result of the large number of coordinating oxygen atoms the cation–oxygen bond distances are long and the bonds are typically weak. The more intermediate-sized transition element cations such as Mn (and usually Fe) are coordinated by fewer oxygen atoms and form slightly shorter bonds. In this study, the network-modifiers exhibit greater sensitivity to the accumulated α-decay dose than do the network-formers. Of the network-modifiers, the cations coordinated by fewer oxygen atoms and with shorter cation–oxygen bonds are more resistant to the effects of radiation damage.

The response of the next-nearest neighbor shells to radiation damage is similar for many of the cations: a decrease in the cation–silicon bond lengths indicating a contraction of the silica tetrahedral units around the cations. This suggests that radiation damage results in structural modification of the silica network. Bulk density measurements of these same glasses have shown a decrease in density with accumulated α-decay dose [28]. These two results suggest that the structural modification of silica network takes the form of changes in the Si–O–Si bond angle between tetrahedral units.

The high accumulated α-decay dose experienced by the ^{238}Pu-doped zircon crystal resulted in amorphization of the zircon structure. Whereas the local Zr environment shows dramatic changes in coordination, the coordination environment around the Pu cation appears to be preserved. The results for the zircon waste form do not follow the trend of radiation resistance demonstrated by the cations in the glass waste form. Future annealing studies of the ^{238}Pu-doped zircon may elucidate the amorphization process in the ceramic waste form.

5. Conclusions

EXAFS studies were performed on aged, Pu-doped borosilicate glass and polycrystalline zircon samples. Analysis of the EXAFS and XANES spectra indicate that the local environment around the cations exhibits different degrees of disorder as a result of the accumulated α-decay dose. In the glass samples, cations with short cation–oxygen bonds show little effect from self-radiation whereas cations with long cation–oxygen bonds show a greater degree of disorder with accumulated α-decay dose. In the zircon samples, the high accumulated α-decay dose resulted in amorphization of the zircon structure, yet the coordination environment around the Pu cation appears to be preserved.

Acknowledgements

The XAS experiments were conducted at Stanford Synchrotron Radiation Laboratory, operated by the US Department of Energy, Office of Basic Energy Sciences. This work was supported by Environmental Management Science Program, Office of Environmental Management, US Department of Energy. The Pacific Northwest National Laboratory is operated by Battelle Memorial Institute for the US Department of Energy under contract DE-AC06-RLO 1830.

References

[1] R.L. Fleischer, Science 207 (1980) 979.
[2] Y. Eyal, R.L. Fleischer, Mater. Res. Soc. Proc. 44 (1985) 687.
[3] W.J. Weber, R.C. Ewing, C.A. Angell, G.W. Arnold, A.N. Cormack, J.M. Delaye, D.L. Griscom, L.W. Hobbs, A. Navrotsky, D.L. Price, A.M. Stoneham, M.C. Weinberg, J. Mater. Res. 12 (1997) 1946.
[4] W.J. Weber, R.C. Ewing, C.R.A. Catlow, T. Diaz de la Rubia, L.W. Hobbs, C. Kinoshita, Hj. Matske, A.T. Motta, M.A. Nastasi, E.H.K. Salje, E.R. Vance, S.J. Zinkle, J. Mater. Res., submitted.
[5] W.J. Weber, J.W. Wald, G.L. McVay, Am. Ceram. Soc. 68 (1985) p. C-253.
[6] W.J. Weber, J. Mater. Res. 5 (1990) 2687.
[7] W.H. McMaster, N. Kerr del Grande, J.H. Mallett, J.H. Hubbell, Calculation of X-ray Cross-Sections, University of California, Livermore, 1969, 350 pp.
[8] J.J. Rehr, S.I. Zabinsky, R.C. Albers, Phys. Rev. Lett. 69 (1992) 3397.
[9] S.I. Zabinsky, J.J. Rehr, A. Ankudinov, R.C. Albers, M.J. Eller, Phys. Rev. B. 52 (1995) 2995.
[10] H. Narita, K. Koto, N. Morimoto, Mineral. J. Jpn. 8 (1977) 329.
[11] M. Catti, G. Gazzoni, G. Ivaldi, G. Zanini, Acta Crystallogr. B 39 (1983) 674.
[12] R.M. Hazen, L.W. Finger, Am. Mineral. 64 (1979) 196.

[13] L.H. Fuchs, E. Gebert, Am. Mineral. 43 (1958) 243.
[14] C. Keller, Nuklenoik 5 (1963) 41.
[15] P.H. Ribbe, Am. Mineral. 64 (1979) 402.
[16] A. Anderson, C. Chieh, D.E. Irish, J.P. Tong, Can. J. Chem. 58 (1980) 1651.
[17] P.G. Eller, G.D. Jarvinen, J.D. Purson, R.A. Penneman, R.R. Ryan, F.W. Lytle, R.B. Greegor, Radiochem. Acta 39 (1985) 17.
[18] J. Petiau, G. Calas, D. Petimaire, A. Bianconi, M. Benfatto, A. Marcelli, Phys. Rev. B 34 (1986) 7350.
[19] G. Calas, G.E. Brown Jr., G.A. Waychunas, J. Petiau, Phys. Chem. Min. 15 (1987) 19.
[20] G.N. Greaves, N.T. Barrett, G.M. Antonini, F.R. Thornley, B.T.M. Willis, A. Steel, J. Am. Chem. Soc., 111, pp. 4313.
[21] B.M. Biwer, L. Soderholm, R.B. Greegor, F.W. Lytle, Mater. Res. Soc Proc. 465 (1997) 229.
[22] J.R. Smyth, D.L. Bish, Crystal Structures and Cation Sites of the Rock-Forming Minerals, Allen and Unwin, Boston, 1988, 332 pp.
[23] G. Calas, J. Petiau, Solid State Comm. 48 (1983) 625.
[24] R.E. Hunn, P.R. Suitch, J. L Pentecost, J. Am. Ceram. Soc. 68 (1985) 285.
[25] F. Farges, G. Calas, Am. Mineral. 76 (1991) 60.
[26] D.L. Griscom, J. Ceram. Soc. Jpn. 99 (1991) 923.
[27] R.C. Ewing, W.J. Weber, F.W. Clinard Jr., Prog. Nucl. Energy 29 (1995) 63.
[28] W.J. Weber, Min., Metal, Mater. Soc. 43 (1991) 35.